



fire
cci

ESA Climate Change Initiative – Fire_cci

D2.1.2 Algorithm Theoretical Basis Document (ATBD) – Sentinel-3

Project Name	ECV Fire Disturbance: Fire_cci
Contract N°	4000126706/19/I-NB
Issue Date	22/04/2020
Version	1.1
Author	Joshua Lizundia-Loiola, M. Lucrecia Pettinari, Emilio Chuvieco
Document Ref.	Fire_cci_D2.1.2_ATBD_S3_v1.1
Document type	Public

To be cited as: Lizundia-Loiola J., Pettinari M.L., Chuvieco E. (2020) ESA CCI ECV Fire Disturbance: D2.1.2 Algorithm Theoretical Basis Document (ATBD) – Sentinel-3, version 1.1. Available at: <https://www.esa-fire-cci.org/documents>

	Fire_cci Algorithm Theoretical Basis Document	Ref.:	Fire_cci_D2.1.2_ATBD_S3_v1.1		
		Issue	1.1	Date	22/04/2020
				Page	2

Project Partners

Prime Contractor/ Scientific Lead & Project Management	UAH – University of Alcalá (Spain)
Earth Observation Team	UAH – University of Alcalá (Spain)
	UPM – Universidad Politécnica de Madrid (Spain)
	CNR-IREA - National Research Council of Italy – Institute for Electromagnetic Sensing of the Environment (Italy)
System Engineering	BC – Brockmann Consult (Germany)
Climate Modelling Group	MPIM – Max Planck Institute for Meteorology (Germany)
	CNRS - National Centre for Scientific Research (France)



Distribution

Affiliation	Name	Address	Copies
ESA	Simon Pinnock (ESA)	simon.pinnock@esa.int	electronic copy
	Clément Albergel	clement.albergel@esa.int	
Project Team	Emilio Chuvieco (UAH)	emilio.chuvieco@uah.es	electronic copy
	M. Lucrecia Pettinari (UAH)	mlucaresia.pettinari@uah.es	
	Joshua Lizundia (UAH)	joshua.lizundia@uah.es	
	Gonzalo Otón (UAH)	gonzalo.oton@uah.es	
	Mihai Tanase (UAH)	mihai.tanase@uah.es	
	Miguel Ángel Belenguer (UAH)	miguel.belenguer@uah.es	
	Consuelo Gonzalo (UPM)	consuelo.gonzalo@upm.es	
	Dionisio Rodríguez Esparragón (UPM)	dionisio.rodriguez@ulpgc.es	
	Ángel García Pedrero (UPM)	angelmario.garcia@upm.es	
	Daniela Stroppiana (CNR)	stroppiana.d@irea.cnr.it	
	Mirco Boschetti (CNR)	boschetti.m@irea.cnr.it	
	Thomas Storm (BC)	thomas.storm@brockmann-consult.de	
	Martin Böttcher (BC)	martin.boettcher@brockmann-cons...	
	Grit Kirches (BC)	grit.kirches@brockmann-consult.de	
Angelika Heil (MPIM)	angelika.heil@mpimet.mpg.de		
Idir Bouarar (MPIM)	idir.bouarar@mpimet.mpg.de		
Florent Mouillot (CNRS)	florent.mouillot@cefe.cnrs.fr		
Philippe Ciais (CNRS)	philippe.ciais@lsce.ipsl.fr		

	Fire_cci Algorithm Theoretical Basis Document	Ref.:	Fire_cci_D2.1.2_ATBD_S3_v1.1		
		Issue	1.1	Date	22/04/2020
					Page

Summary

This Algorithm Theoretical Basis Document describes the analyses that were made to select the most suitable product to generate a moderate spatial resolution global burned area product for the Fire_cci project based on Sentinel-3 data.

	Affiliation/Function	Name	Date
Prepared	UAH	Joshua Lizundia-Loiola	22/04/2020
Reviewed	UAH – Project Manager	Lucrecia Pettinari	22/04/2020
Authorized	UAH - Science Leader	Emilio Chuvieco	22/02/2020
Accepted	ESA - Technical Officer	Clément Albergel	23/04/2020

This document is not signed. It is provided as an electronic copy.

Document Status Sheet

Issue	Date	Details
1.0	30/03/2020	First Version of the document
1.1	22/04/2020	Addressing comments of Fire_cci+_D2.1.2_ATBD_S3_v1.0_RID.doc

Document Change Record

Issue	Date	Request	Location	Details
1.1	22/04/2020	ESA	Sections 2, 3.1, 3.1.2 Section 3.2	Small changes in the text. Caption of figure 1 expanded.

Table of Contents

1	Executive Summary	6
2	Introduction and objectives.....	6
3	Methodology	7
3.1	Input data	7
3.1.1	Sentinel-3 OLCI with iCOR atmospheric correction (OLCI iCOR).....	7
3.1.2	Sentinel-3 SLSTR Top-of-Atmosphere reflectance (SLSTR TOA)	9
3.1.3	Sentinel-3 Synergy (SYN).....	10
3.2	Test datasets design	10
3.3	FireCCI51 global BA algorithm	12
3.4	Criteria to assess the suitability of input datasets	12
4	Results and discussion	14
4.1	Availability and stability of the time series	14
4.2	Sensitivity to burned pixels' detection.....	16
4.3	BA classification.....	17
5	Conclusion.....	19
6	References	20
	Annex 1 Acronyms and abbreviations.....	21
	Annex 2 Accuracy measures for the sample of 2019	22
	Annex 3 Intercomparison	24

List of Tables

Table 1.	Bands of the Sentinel-3 OLCI (https://sentinel.esa.int/web/sentinel/user-guides/sentinel-3-olci/resolutions/radiometric , last accessed March 2020). MERIS heritage bands in orange.	8
Table 2.	Bands of the Sentinel-3 SLSTR (https://sentinel.esa.int/web/sentinel/user-guides/sentinel-3-slstr/resolutions/radiometric , last accessed march 2020). AATSR heritage bands in orange.	9
Table 3.	Bands selected from each input dataset for BA detection.	12
Table 4.	Estimated accuracy of each dataset and band.....	22
Table 5.	R2 of the spatial correlation between datasets.	25
Table 6.	Slope of the spatial correlation between datasets.	25

List of Figures

Figure 1.	The 13 study sites (in orange) used for the testing of the three datasets. A total of 273 tiles will be processed in the final global BA product.....	11
Figure 2.	Validation sites distributed among the thirteen study sites.....	13
Figure 3.	Number of valid observations of OLCI iCOR and SYN and their difference per tile. Each tile boxplot shows the distribution of all its pixels (3600x3600 pixels).....	14
Figure 4.	Reflectance time series for the bands listed on Table 3 from the 1st of January to the 31st of May of 2019 of the two points indicated in (e). The points are located on deserted areas.	16

Figure 5. Reflectance time series for the bands listed on Table 3 from the 1st of January to the 31st of May of 2019 of two points indicated in (e). The points were located in burned areas during that period. 17

Figure 6. Dice coefficient of the results derived from applying the FireCCI51 algorithm (Section 3.3) to the 865 nm band, which is provided by different products. Accuracy metrics can be found in Annex 2, Table 4..... 18

Figure 7. BA in km² per tile (top) and month (down) detected by the NIR band centred at 865 nm (868 nm for SYN SLSTR) provided by OLCI iCOR, SYN OLCI, SYN SLSTR and OLCI C3S. 18

Figure 8. BA in km² per tile (top) and month (down) detected by each band of the OLCI iCOR product..... 24

Figure 9. BA in km² per tile (top) and month (down) detected by each band of the SYN product..... 24

	Fire_cci Algorithm Theoretical Basis Document	Ref.:	Fire_cci_D2.1.2_ATBD_S3_v1.1			
		Issue	1.1	Date	22/04/2020	
					Page	6

1 Executive Summary

This is the first version of the Algorithm Theoretical Basis Document (ATBD) describing the algorithm to be used to generate the Fire_cci Sentinel-3 Synergy product version 1.0 (FireCCIS310) global burned area (BA) product. As a result of the problems faced to obtain good quality Synergy (SYN) data to comply with the time series (2017-2019), this document explores different alternatives to obtain BA data from the Sentinel-3 sensors. The current version shows all the analyses that have been performed to identify and select the most suitable product that will be used to generate the FireCCIS310 product. The next version of the ATBD will focus on the description of the final BA algorithm.

2 Introduction and objectives

The ESA Climate Change Initiative (CCI) stresses the importance of providing a higher scientific visibility to data acquired by ESA sensors, especially in the context of the Intergovernmental Panel on Climate Change (IPCC) reports. This implies producing consistent time series of accurate Essential Climate Variable (ECV) products, which can be used by the climate, atmospheric and ecosystem scientists for their modelling efforts. The importance of keeping long-term observations and the international links with other agencies currently generating ECV data is also stressed.

Fire Disturbance is one of the ECVs mainly due to fire impacts on emissions calculation and carbon budgets. The Fire disturbance ECV identifies BA as the primary fire variable. Accordingly, the Fire_cci project focuses on developing and validating algorithms to meet the Global Climate Observing System (GCOS) ECV requirements for (consistent, stable, error-characterised) global satellite data products from multi-sensor data archives.

The first algorithm developed within the project used images from the MERIS sensor (Alonso-Canas and Chuvieco 2015). Due to the availability of images from this sensor, the time series of the MERIS Fire_cci v4.1 (FireCCI41 to simplify) product only covered the years 2005-2011 (Chuvieco et al., 2016). A new product was released two years later, based on the MODIS sensor (FireCCI50) that extended that time series to the period 2001-2016 (Chuvieco et al., 2018). The algorithm to obtain this product was developed for the two highest-spatial resolution bands of the MODIS sensor (Red and Near Infrared, NIR) and followed a similar approach to the MERIS hybrid algorithm, as it combined information from hotspots and temporal reflectance changes to detect burned pixels. Differences in the characteristics of both sensors and their derived products (spatial and temporal resolution, view angles, bands characteristics, etc.) and problems found with FireCCI41 product advised to extend previous developments and introduce some adaptations for that MODIS BA algorithm, which improved both the thematic and temporal accuracy of the product. Nevertheless, a few artefacts were still observed in the FireCCI50 product, which were related to the tile-based thresholding approach. Thus, the last version of the algorithm introduced a cluster-based thresholding approach (Lizundia-Loiola et al., 2020). This algorithm was the basis to produce the latest version of the global BA product (FireCCI51), which showed better accuracy than previous versions.

The FireCCI51 algorithm is the starting point for the development of the new FireCCIS310 algorithm that initially was going to be applied to the 2017-2019-time series of Sentinel-3 Synergy (SYN) data, following the technical annex submitted to ESA. However, on April 2019, when the kick off meeting of the Fire_cci project was held in Alcalá de Henares (Spain), doubts were expressed on whether SYN data had enough quality and temporal availability to proceed with the original plans. At that moment, SYN was only available since October 2018. After several discussions with ESA officers in charge of the SYN

	fire cci	Fire_cci		Ref.: Fire_cci_D2.1.2_ATBD_S3_v1.1
		Algorithm Theoretical Basis Document		Issue 1.1 Date 22/04/2020
				Page 7

processing chain in the following months, still SYN data was not yet readily available and with the acceptable level of input quality. Therefore, it was decided to explore other alternatives from Sentinel-3 sensors in October 2019, during the first Progress Review Meeting (PRM). Two decisions were made to advance on the generation of the global moderate resolution BA product for the current Fire_cci contract: the time series of the FireCCIS310 was changed from 2017-2019 to 2019-2020 and two alternatives to SYN data were going to be explored (OLCI and SLSTR). The former decision implied that the golden year initially decided to compare coarse and medium resolution products was changed from 2018 to 2019. This also implied that the FireCCI51 product had to be extended to 2019 to compare outputs with S-3 and AVHRR Long-Term Data Record (LTDR) based products. As for the alternative inputs for the new S-3 BA product, it was decided to perform an analysis on which of the following three Sentinel-3 products was the most suitable to be the input for the FireCCIS310 algorithm: OLCI with iCOR atmospheric correction (Level 2), SLSTR Top-Of-Atmosphere (TOA) reflectance (Level 1B), or SYN data (Level 2).

The objective of comparing those three datasets was to check whether SYN data were stable, but sensitive enough, to detect BA and compare the stability and sensitivity of these data to those offered by OLCI and SLSTR. The final goal was to select which input product was more suitable for detecting burned pixels and therefore which one should be used to generate the FireCCIS310 global BA algorithm. This version of the ATBD presents the results of that analysis and the conclusions that have been reached about which of the above mentioned products will be used to generate the FireCCIS310 product.

3 Methodology

3.1 Input data

Sentinel-3 is primarily an ocean mission, but it is able to provide atmospheric and land applications as well, providing data continuity to the ERS, ENVISAT, SPOT and PROBA-V satellites (<https://sentinel.esa.int/web/sentinel/missions/sentinel-3>, last accessed March 2020). The first Sentinel-3 (A) was launched on February 2016 and the second (B) was launched on April 2018 on the same orbit but flown $\pm 140^\circ$ out of phase. The orbit is sun-synchronous, with a height of 814.5 km, an inclination of 98.65° and a repeat cycle of 27 days, crossing the equator at around 10:00 am. It includes seven main instruments: OLCI, SLSTR, SRAL, MWR, DORIS, LRR and GNSS.

As mentioned in the previous section two Sentinel-3 datasets were proposed as alternatives for SYN data (Section 3.1.3): OLCI reflectance with iCOR atmospheric correction (Section 3.1.1) and SLSTR TOA reflectance (Section 3.1.2).

3.1.1 Sentinel-3 OLCI with iCOR atmospheric correction (OLCI iCOR)

OLCI simultaneously measures the solar radiation reflected by the Earth in 21 spectral bands from 400 nm to 1020 nm (Table 1). Each of these bands is programmable in position and width. Like its predecessor MERIS, OLCI was originally conceived for oceanographic applications, particularly to retrieve ocean colour. For this reason, the sensor incorporates several bands in the blue and green regions of the electromagnetic spectrum, as they are closely related to chlorophyll content. As OLCI was mainly designed for ocean monitoring, the instrument is capable of detecting the low levels of radiation emerging from the water constituents. However, at the same time, the instrument has a high dynamic range to detect bright objects (clouds, snow).

It is a push-broom instrument with 5 camera modules sharing the field of view (FOV), each one with a FOV of 14.2° and 0.6° overlap with its neighbours. The whole FOV is shifted across track by 12.6° away from the Sun to minimise the impact of sun glint. It has a swath of 1270 km (FOV = 68.6°), and a native spatial resolution of ~300 m. OLCI allowed global coverage of the Earth land colour in 2.2 days with one satellite and 1.1 with two.

Table 1. Bands of the Sentinel-3 OLCI (<https://sentinel.esa.int/web/sentinel/user-guides/sentinel-3-olci/resolutions/radiometric>, last accessed March 2020). MERIS heritage bands in orange.

Band	λ centre (nm)	Width (nm)	Function
Oa01	400	15	Aerosol correction, improved water constituent retrieval
Oa02	412.5	10	Yellow substance and detrital pigments (turbidity)
Oa03	442.5	10	Chlorophyll absorption maximum, biogeochemistry, vegetation
Oa04	490	10	High Chlorophyll,
Oa05	510	10	Chlorophyll, sediment, turbidity, red tide
Oa06	560	10	Chlorophyll reference (Chlorophyll minimum)
Oa07	620	10	Sediment loading
Oa08	665	10	Chlorophyll (2nd Chlorophyll absorption maximum), sediment, yellow substance/vegetation
Oa09	673.75	7.5	For improved fluorescence retrieval and to better account for smile together with the bands 665 and 680 nm
Oa10	681.25	7.5	Chlorophyll fluorescence peak, red edge
Oa11	708.75	10	Chlorophyll fluorescence baseline, red edge transition
Oa12	753.75	7.5	O2 absorption/clouds, vegetation
Oa13	761.25	2.5	O2 absorption band/aerosol correction.
Oa14	764.375	3.75	Atmospheric correction
Oa15	767.5	2.5	O2A used for cloud top pressure, fluorescence over land
Oa16	778.75	15	Atmos. corr./aerosol corr.
Oa17	865	20	Atmospheric correction/aerosol correction, clouds, pixel co-registration
Oa18	885	10	Water vapour absorption reference band. Common reference band with SLSTR instrument. Vegetation monitoring
Oa19	900	10	Water vapour absorption/vegetation monitoring (maximum reflectance)
Oa20	940	20	Water vapour absorption, Atmospheric correction/aerosol correction
Oa21	1 020	40	Atmospheric correction/aerosol correction

OLCI has the capability to output data sampled at the Full Resolution (FR) with the spatial sampling described above, and Reduced Resolution (RR) data sub-sampled at 1.2 km (averaging the signal of a grid of 16 FR pixels). The following Level 1B products are available at ESA:

- OLCI Full Resolution calibrated, ortho-geolocated and spatially re-sampled TOA radiances (OL_1_EFR).

- OLCI Reduced Resolution calibrated, ortho-geolocated and spatially re-sampled TOA radiances (OL_1_ERR).

In our case, the OL_1_EFR was atmospherically corrected using the iCOR software (<https://remotesensing.vito.be/case/icor>, last accessed march 2020). A validation of the software can be found in De Keukelaere et al. (2018). To extend the original state QA flags the pixel identification tool of Brockman Consult (BC) called idepix was also applied. This allowed to filter out, in addition to clouds, cloud shadows.

3.1.2 Sentinel-3 SLSTR Top-of-Atmosphere reflectance (SLSTR TOA)

The Sea and Land Surface Temperature Radiometer (SLSTR) is a dual view (near-nadir and backward views) conical imaging radiometer aboard Sentinel-3 satellites, which provides continuity to the ENVISAT AATSR instrument. Its dual view scan has a swath width of 1420 km at nadir and 750 km backwards allowing two simultaneous observations in nadir view and oblique view, respectively.

The SLSTR has 6 bands in the visible and Short-Wave Infrared (SWIR) bandwidths with a resolution of 500 m, and another 3 bands in the medium and thermal infrared with 1000 m of spatial resolution. Also, the F1 and F2 fire bands are based on the same detectors as S7 and S8 but with an increased dynamic range to minimise saturation over fires (Table 2). The following Level 1B products are available at ESA:

- Level-1B product: provides TOA radiances and brightness temperatures for each pixel in the instrument grid, each view (nadir and oblique), and each SLSTR channel, plus annotations data associated with SLSTR pixels (SL_1_RBT).

Table 2. Bands of the Sentinel-3 SLSTR (<https://sentinel.esa.int/web/sentinel/user-guides/sentinel-3-slstr/resolutions/radiometric>, last accessed march 2020). AATSR heritage bands in orange.

Band	λ centre (nm)	Width (nm)	Function	Comments		Spatial resolution (metres)
S1	554.27	19.26	Cloud screening, vegetation monitoring, aerosol	VNIR	Solar Reflectance Bands	500
S2	659.47	19.25	NDVI, vegetation monitoring, aerosol			
S3	868.00	20.60	NDVI, cloud flagging, Pixel co-registration			
S4	1374.80	20.80	Cirrus detection over land	SWIR		
S5	1613.40	60.68	Cloud clearing, ice, snow, vegetation monitoring			
S6	2255.70	50.15	Vegetation state and cloud clearing			
S7	3742.00	398.00	SST, LST, Active fire	Thermal IR Ambient bands (200 K -320 K)		1000
S8	10854.00	776.00	SST, LST, Active fire			
S9	12022.50	905.00	SST, LST			
F1	3742.00	398.00	Active fire	Thermal IR fire emission bands		
F2	10854.00	776.00	Active fire			

This product was transformed from TOA radiances to TOA reflectance by BC. Initially, in the Visible/NIR/SWIR channels ESA official calibration process the digital numbers are first converted to reflectance, because the cloud identification step performs processing on brightness temperatures and reflectance (<https://sentinel.esa.int/web/sentinel/technical->

	Fire_cci Algorithm Theoretical Basis Document	Ref.:	Fire_cci_D2.1.2_ATBD_S3_v1.1		
		Issue	1.1	Date	22/04/2020
				Page	10

[guides/sentinel-3-slstr/level-1/signal-calibration](#), last accessed March 2020). However, these reflectance values are converted to radiance in the next step and delivered as radiances to the final user. Therefore, BC needed to apply a backwards conversion using formulas given on the SLSTR ATBD (Birks et al., 2011) to obtain “again” the reflectance, which is the variable used as inputs in the BA algorithms.

3.1.3 Sentinel-3 Synergy (SYN)

The Synergy data was created with the aim of ensuring continuation of the SPOT-VGT products. For doing so, both OLCI and SLSTR bands are resampled to a common OLCI grid at ~300m, atmospherically corrected and included in a unique Level 2 product. Since none of the previously mentioned sensors have its own surface directional reflectance product, Synergy was also a way of providing such information to the user. Several SYN products are delivered:

- Level-2 SYN product (SY_2_SYN): contains surface reflectance and aerosol parameters over land, provided on the OLCI image grid (~300m), for the sun-reflective channels of SLSTR (both in nadir and oblique view), except band S4, and all OLCI channels, except bands Oa14, Oa15 and Oa20.
- Level-2 VGP product (SY_2_VGP): contains TOA reflectances at 1 km spatial resolution, provided on a regular latitude-longitude grid (called 1 km VGT-like product).
- Level-2 VG1 product (SY_2_VG1): contains a daily synthesis of surface reflectance, with the spatial resolution of the 1 km VGT-like product, based on information of the same channels of SPOT-VGT (B0, B2, B3 and Middle Infrared) produced with OLCI and SLSTR data. It also contains Normalized Difference Vegetation Index (NDVI) information.
- Level-2 VG10 product (SY_2_VG10): similar to the VG1, but with a 10-day synthesis surface reflectances and NDVI.

In our case, the scientific content SY_2_SYN is not modified since the product already offers what is required by the algorithm (surface directional reflectance).

3.2 Test datasets design

The decision to perform the comparison among the three alternatives was made after the first PRM (October 2019) and, hence, the temporal coverage of the test datasets was set from January to September of 2019. The idea was to produce BA results from March to August, although the most stable results belonged to summer of that year (June, July and August), which partially matches the fire season of most of the testing sites.

Regarding the spatial distribution of the data, since ESA provides all the aforementioned products in strips, an internal tiling system that divides the Earth burnable areas in 273 tiles of 10x10° degrees was proposed within the Fire_cci project based on the knowledge acquired during the MERIS processing (Figure 1). Therefore, the original data was pre-processed by BC to split the information into those tiles. When more than one valid observation was available for the same pixel, e.g. when Sentinel-3 A and B observations are available or in high latitudes, the most nadiral observation was selected based on the sensor’s View Zenith Angle (VZA), that is, OLCI VZA in the case of OLCI iCOR and SLSTR VZA in the case of SLSTR TOA. In the case of Synergy, which includes both OLCI and SLSTR bands, the OLCI VZA was used in all the cases. The SLSTR VZA might have been used for the corresponding SLSTR bands. However, the combination of OLCI and SLSTR measurements from different observations could have resulted in artificial not

occurring spectra, e.g. OLCI measurements from vegetated area and SLSTR measurement from shaded or rained vegetated area. Furthermore, the BRDF effect and also the geolocation accuracy could influence the resulting spectra in this case.

Thirteen of those tiles that represent a wide range of vegetation types and fire regimes (Figure 1) were selected to test the quality of the three input products and their aptitude for BA detection. These areas are the equivalent of the 10 MODIS sinusoidal tiles that were used for the FireCCI51 algorithm development (Lizundia-Loiola et al., 2020).

Two tiles were located in the North Australian region (h30v10 and h31v10). This region is strongly dominated by tropical savannah, in which fire is a fundamental management tool (Stroppiana et al. 2003). As an example of the boreal forest, two test tiles were located in Canada (h06v03 and h07v03). In the case of temperate forests, two tiles from the western coast of the United States were chosen (tile h05v05 and h06v05).

Another seven tiles were used from areas that were identified in previous phases as particularly problematic. One of the problems identified in those tiles was the sensitivity of tile-based thresholds to different land covers (Angola, h19v10). Potential border effects were analysed between tiles in Central Africa (h19v07 and h19v08). A Kazakhstan tile (including regions of Uzbekistan and Turkmenistan) (h24v04) was selected as it may cause region-growing problems because of the high BA/HS ratio found in that area (Hantson et al. 2013). A tile in Colombia (h10v08) was chosen because of being a transition zone between grasslands and the Andean forest. Finally, two tiles located in the Russian far eastern area (h30v03 and h31v03), in the north border with China, were selected, which is affected by huge fires almost every year during spring (Kobayashi et al. 2007).

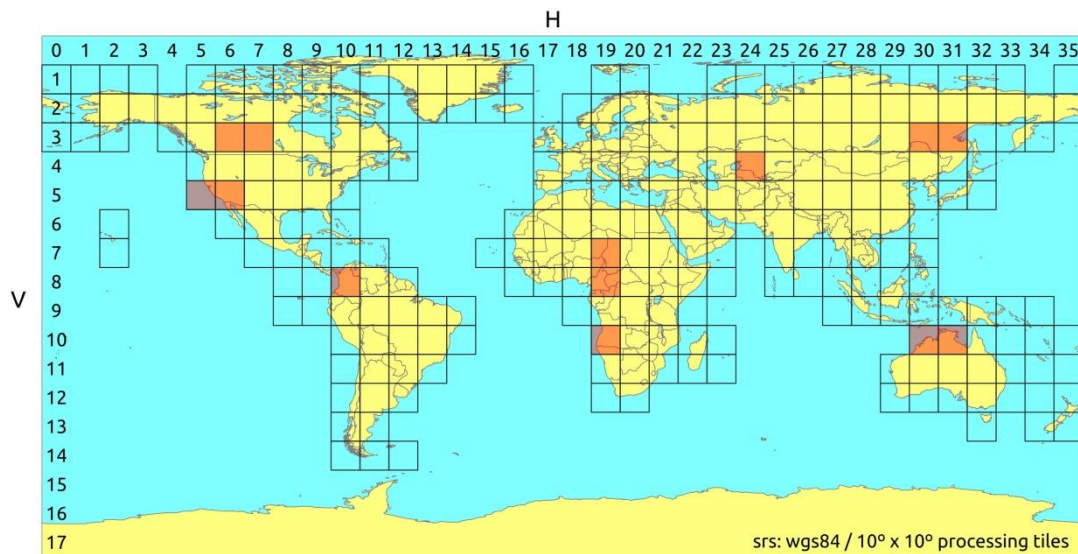


Figure 1. The 13 study sites (in orange) used for the testing of the three datasets. A total of 273 tiles will be processed in the final global BA product (marked with the squares).

As mentioned in Section 3.1 both OLCI and SLSTR data provide more bands than those that are actually needed for BA detection. Therefore, some specific bands that have the potential to detect BA were selected to reduce the size of the input images (Table 3).

Table 3. Bands selected from each input dataset for BA detection.

Band	λ centre (nm)	Spectral region	Justification	Dataset		
				OLCI iCOR	SLSTR TOA	SYN
Oa12	753.75	NIR	Used by FireCCI41 (Alonso-Canas and Chuvieco 2015)	X		X
Oa17	865.00		Used by FireCCI51 (Lizundia-Loiola et al., 2020)	X		X
S3	868.00		Similar to Oa17		X	X
S5	1613.40	SWIR	Used by FireCCISFD11 (Roteta et al., 2019)		X	X
S6	2255.70		Used by FireCCISFD11 (Roteta et al., 2019)		X	X

3.3 FireCCI51 global BA algorithm

To test the suitability of the different input datasets, we followed the same approach applied to the previous version of the algorithm (the one used to create the FireCCI51 product). The structure of this algorithm follows a hybrid approach, using both thermal anomalies information and NIR reflectance values from Terra satellite's MODIS sensor. Thermal anomalies are used to identify active fires, as they have high thermal contrast with the background. The change in reflectance is used to detect the whole burned patch since it is temporally more persistent.

The algorithm uses a two-phase methodology. First, pixels that have a high probability of being burned, called 'seeds', are chosen using restrictive spectral conditions (to reduce commission errors). Those candidate 'seed' pixels are derived from MODIS thermal anomalies considering the relative drop in NIR reflectance. Then a contextual region growing is applied from the 'seeds' to entirely detect the burned patch, in order to reduce the omission errors. Before selecting the seeds, monthly temporal NIR composites are created to reduce noise caused by clouds, cloud shadows, and different artefacts. Two variables are used for BA detection: NIR post-fire values, given by the monthly composites, and the relative change between consecutive NIR composites values.

To guide both the seed and region-growing phases FireCCI51 uses a cluster-based thresholding, which identifies burned-unburned thresholds of reflectance from values of spatially-aggregated active fires and its surroundings.

More information about the algorithm can be found in Lizundia-Loiola et al., 2020.

3.4 Criteria to assess the suitability of input datasets

Two different assessments were performed with the three datasets provided by BC. In a first step, the quality of the dataset itself was analysed by computing the stability of the reflectance time series, its sensitivity to the burn signal, and the number of valid observations that were available for each dataset. In a second step, the quality of the BA detection was assessed by applying the FireCCI51 algorithm to the different input bands of different datasets and then comparing the results with validation data.

The analysis of reflectance was visually done by checking the time series (01/01/2019 – 30/09/2019) of some points distributed among spectrally stable land covers (e.g. deserts or locations with sparse vegetation). This allowed comparing between datasets to verify which of them was more affected by angular effects (BRDF related problems). To visually check

the sensitivity of the inputs to the burned signal, reflectance time series of some burned pixels were extracted. The location of those pixels was guided by the validation dataset described in the following paragraph.

For assessing the BA results, three analyses were performed. On the one hand, the BA results of each band and dataset were compared with a proper validation dataset that was generated for the study sites. Following the approach described in Stroppiana and Boschetti (2019) 44 validation sites of 100x100 km were generated based on Landsat 8 OLI images at 30 m resolution (Figure 2). All the reference perimeters were derived from the April-August period, when possible. The validation sites were not statistically sampled, but visually selected to ensure interpretability of the Landsat scenes. The mathematical expressions of the accuracy metrics that are used in the validation can be found in Stroppiana and Boschetti (2019), i.e. commission error (Ce), omission error (Oe), Dice coefficient (DC) and relative bias (relB). No reference perimeters were available for Colombia (h10v08) since the fire season lasts from December to March. On the other hand, the BA results of the March – August period derived from different bands and datasets were compared taking into account the amount of BA detected and the spatial correlation of burned patches in 0.05x0.05-degree grid cells. Finally, an intercomparison with an existing global BA product was made. For that purpose, the new operational global BA product of the Copernicus Climate Change Service (C3S) was selected, which time series goes from January 2017 to October 2019. This product, called C3SBA10, is based on the algorithm described on Section 3.3 and it uses the MODIS active fires as well as Sentinel-3's OLCI 300m resolution 865 nm NIR band to detect BA. The difference between the OLCI reflectance used by this global BA product and the one considered in this document is the atmospheric correction (AC). In the case of the C3S project, the MERIS AC approach was adapted to correct OLCI data. This method was developed during the GlobAlbedo project (Lewis et al. 2012). A major difference between the iCOR and the C3S AC methods is the aerosol retrieval. C3S OLCI AC retrieves the aerosol optical depth (AOD) from the measurements itself and provides an AOD per pixel. The OLCI iCOR uses one retrieved AOD per tile. The C3SBA10 product can be downloaded from the Climate Data Store (<https://cds.climate.copernicus.eu/cdsapp#!/dataset/satellite-fire-burned-area?tab=overview>, last accessed March 2020).

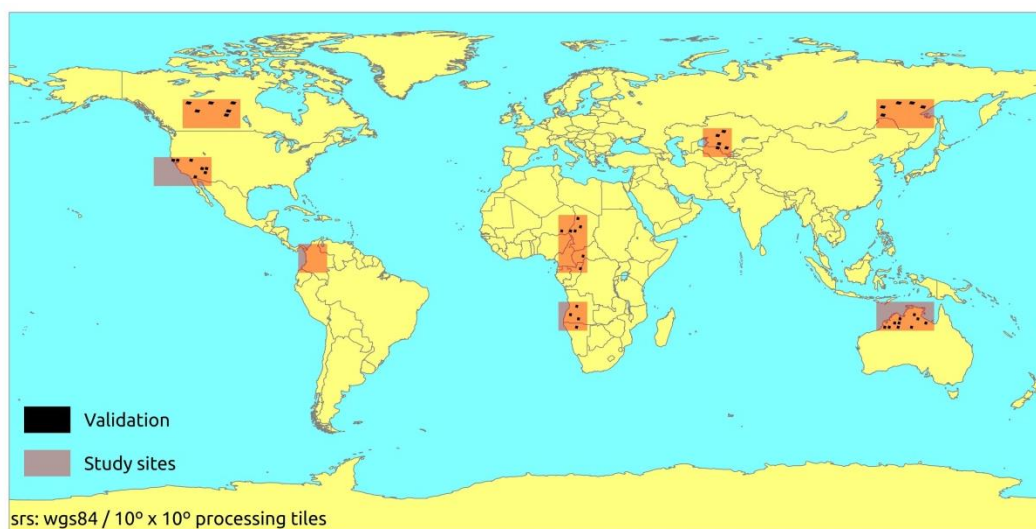


Figure 2. Validation sites distributed among the thirteen study sites.

4 Results and discussion

4.1 Availability and stability of the time series

The box plots in

Figure 3 show the number of valid observations for OLCI iCOR (top), SYN (middle) and the difference between them (bottom), computed analysing each of the pixels (3600x3600) of each tile. The maximum number of valid images is 273 (01/01/2019 - 30/09/2019), meaning that a particular pixel was observed during all the days of that period. If the value is lower, it represents that that pixel was not observed in some of those dates, due to cloud cover, sensor failure, etc. Trends are similar for both products. Tiles located at the tropical savannah of Northern Australia (h30v10, h31v10), Central Africa (h19v07) and Angola (h19v10), at the shrublands of Kazakhstan (h24v04), and the temperate area of California (h05v05, h06v05) have the highest number of observations. Conversely, the boreal areas (h06v03, h07v03) of North America and Amur, Far East Russia (h30v03, h31v03), along with the tropical forested areas of Colombia (h10v08) and Cameroun (h19v08) have the lowest.

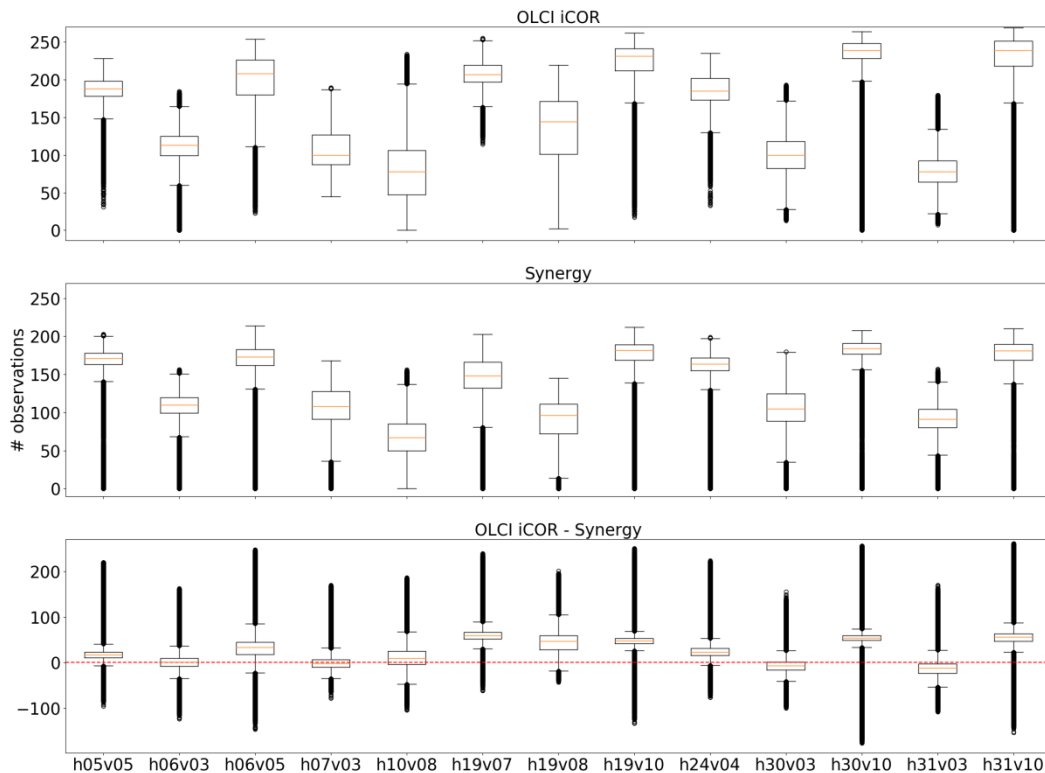


Figure 3. Number of valid observations of OLCI iCOR and SYN and their difference per tile. Each tile boxplot shows the distribution of all its pixels (3600x3600 pixels)

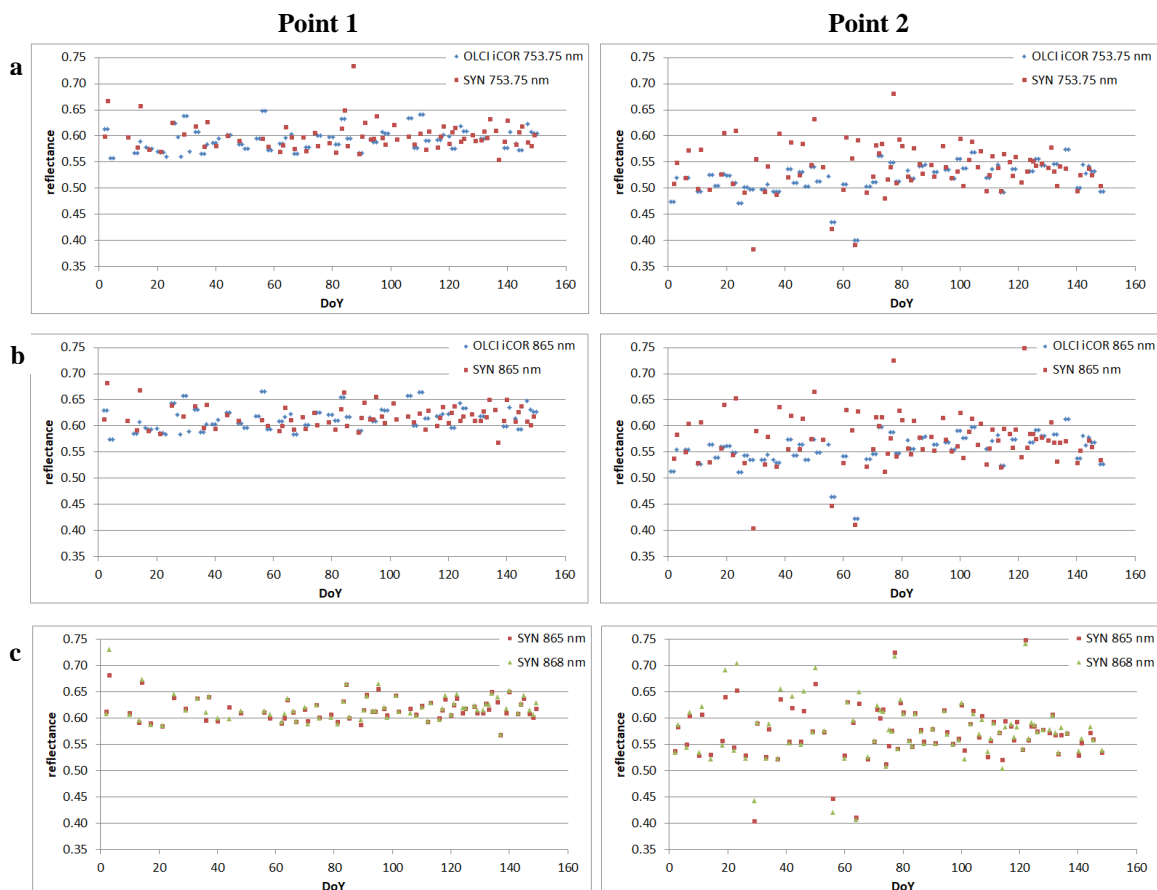
If we observe the median values of the available images for each site, OLCI iCOR presents 239, 239, 207, 231, 185, 188, 208, 113, 100, 100, 78, 78, and 144 valid observations, respectively, while SYN data show -54, -56, -59, -48, -23, -17, -34, -2, +2, +7, +12, -10, and -47 less (-) or more (+) images for the same areas. It is worth mentioning the special case of the two tiles located at Amur (h30v03, h31v03) where SYN presents more observations than OLCI iCOR because in the latter the wintry snow is filtered as cloud. The case of boreal North America, which practically presents the same coverage for both products, is interesting as well. Therefore, in general terms, SYN data have lower temporal

frequency than OLCI iCOR. It seems that, although the original Level 1B data for both products is the same, the complex processing of SYN data applies a more restrictive approach to get the final product.

Regarding SLSTR TOA, BC found several problems to provide the dataset. The most important was the fact that most of the Level 1B images were found to be broken. Only 17 images were delivered for three tiles and 5 images for another one. The rest of tiles were not provided. Taking this into account it was decided to drop this dataset from the analysis.

Regarding the stability of the reflectance trends, the full time series extracted for some deserted and sparsely vegetated areas of the Saharan region showed quite stable reflectance values for both SYN and OLCI iCOR bands in most of the cases. However, some cases were found where SYN data showed a higher variability than OLCI iCOR. Figure 4 contains the time series of two points that represent these two situations. In the case of Point 1, a stable time series can be observed for both SYN and OLCI iCOR bands. However, Point 2 presents much higher variability in the case of the former than in the latter. The same trend can be observed for all NIR (a, b and c) and SWIR (d) bands of SYN. One of the hypotheses of such variability could be that SYN AC uses a more accurate AC when SLSTR oblique view is available, so this could be affecting the reflectance values.

Besides, it was noticed that there was no significant difference between the reflectance values among NIR bands of different wavelengths within a same product. In the case of OLCI iCOR using 753.75nm (a) reflectance seemed to be similar to using the 865nm (b) one. The same was observed for the SYN data where three NIR bands can be found: OLCI's 753.75nm (a) and 865nm (b, c), and SLSTR's 868nm (c). The reflectance trends of the three bands were found to be quite similar.



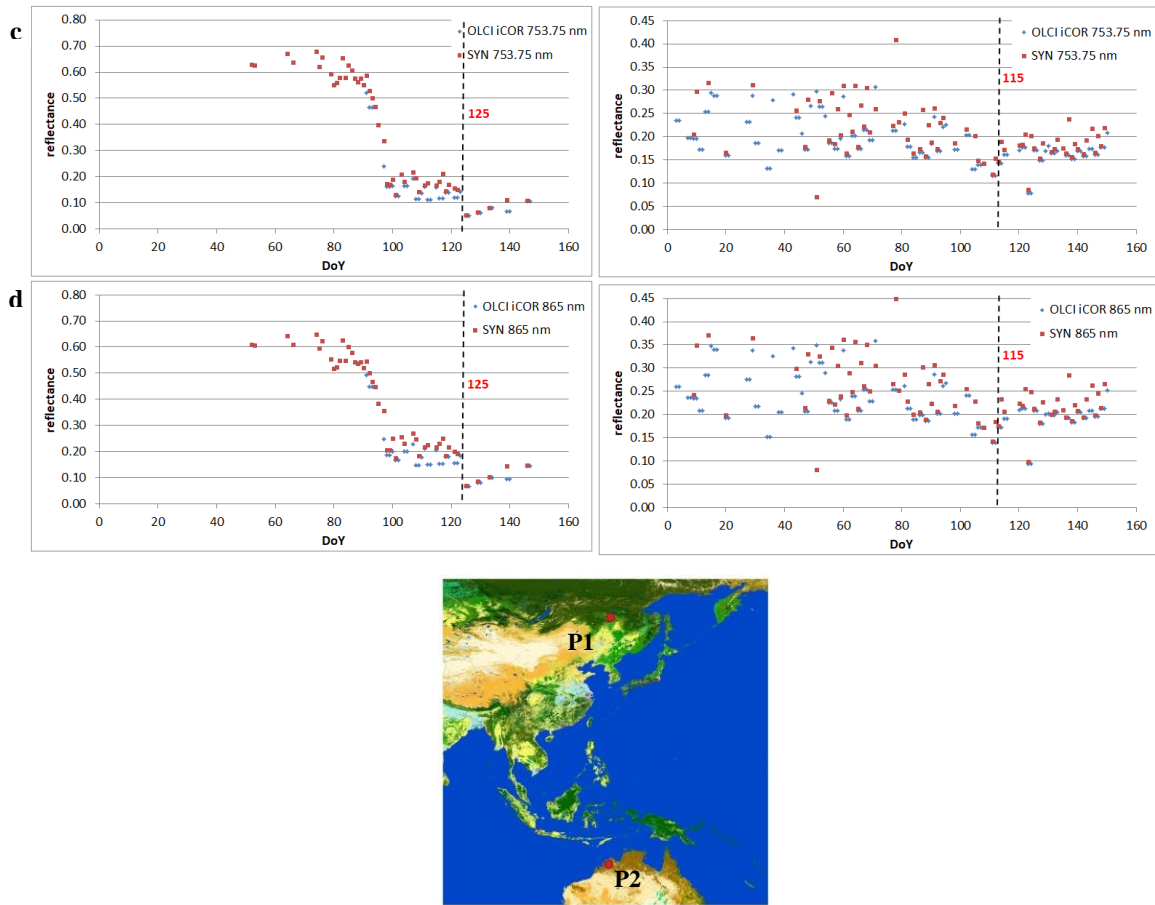


Figure 5. Reflectance time series for the bands listed on Table 3 from the 1st of January to the 31st of May of 2019 of two points indicated in (e). The points were located in burned areas during that period.

4.3 BA classification

The FireCCI51 algorithm was applied without changes to all the bands listed in Table 3, except from those provided by the SLSTR TOA product. The results were validated against 44 validation sites distributed through the study sites (Section 3.4). Besides, they were compared to each other and also to the C3SBA10 global BA product.

Figure 6 compares the accuracy of the results derived from the NIR band centred at 865 nm (868 in the case of SYN SLSTR) provided by different products, i.e. OLCI iCOR, SYN OLCI, SYN SLSTR and OLCI C3S. Figure 7 compares the same datasets but taking into account the amount of BA in km². More information about the validation and intercomparison can be found in Annex 2 and Annex 3, respectively.

Both the validation and intercomparison confirmed that there is no significant difference between using NIR bands centred at different wavelengths that are provided by the same sensor (0, Figure 8 and Figure 9). In the case of OLCI iCOR, the global difference of the Dice coefficient of the NIR bands was lower than 0.2% while for SYN was found to be lower than 0.8% when using any of the three NIR bands (Annex 2, Table 4).

The global accuracy metrics showed a higher capability of SYN NIR data for detecting BA than OLCI iCOR NIR, being the difference on the Dice coefficient of almost 3%. Although OLCI iCOR has more valid observations per pixel than SYN, it seems that the use of composites for BA detection reduces the impact of the mentioned issue. Besides, SYN showed a similar performance of that presented by the global BA product C3SBA10, with

a Dice coefficient of 70.26% and 71.54%, respectively. Although the SYN SWIR bands performed poorly through the study sites, this was expected since the FireCCI51 algorithm was developed to be based on NIR.

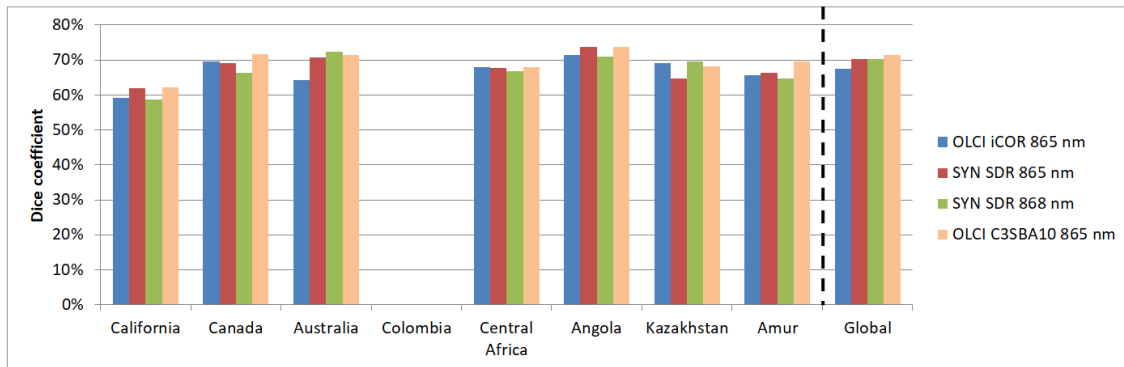


Figure 6. Dice coefficient of the results derived from applying the FireCCI51 algorithm (Section 3.3) to the 865 nm band, which is provided by different products. Accuracy metrics can be found in Annex 2, Table 4.

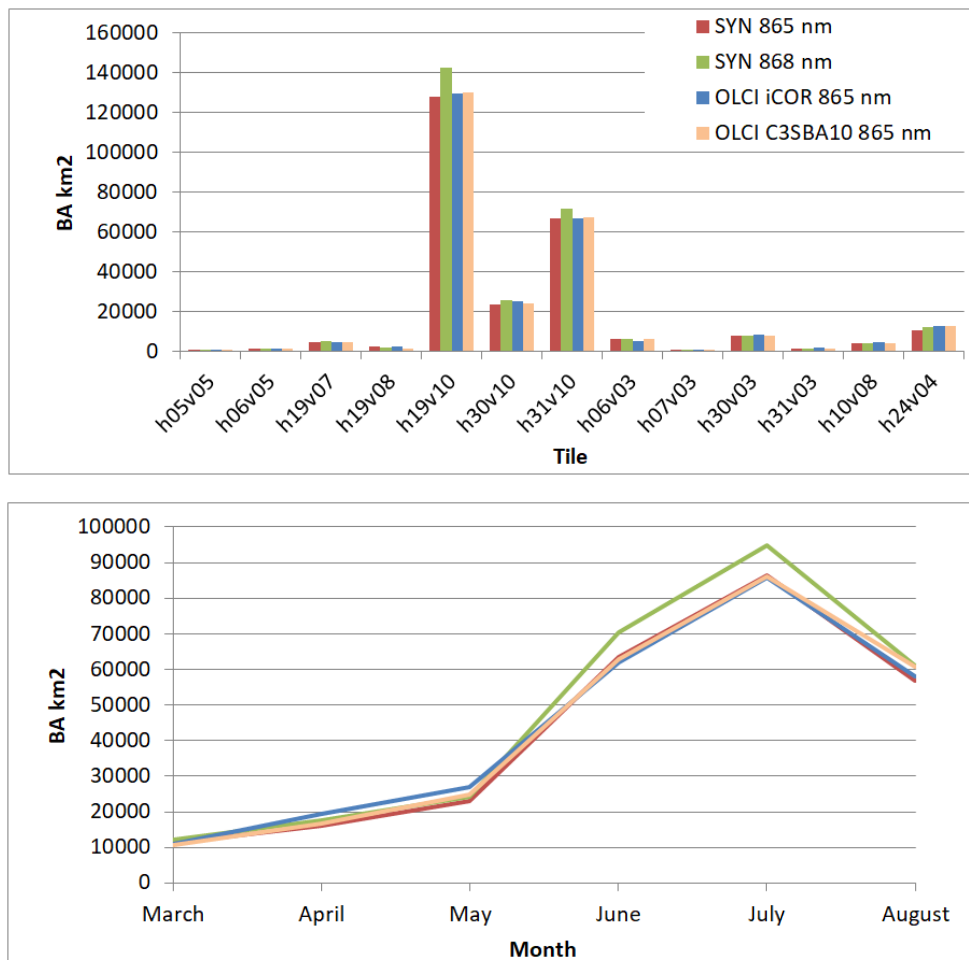


Figure 7. BA in km² per tile (top) and month (down) detected by the NIR band centred at 865 nm (868 nm for SYN SLSTR) provided by OLCI iCOR, SYN OLCI, SYN SLSTR and OLCI C3S.

It is worth noting that the SYN NIR band centred at 868 nm, which has an original resolution of 500 m, shows a similar performance of the 865 nm channel, which has an original resolution of 300 m. In fact, the 868 nm band, which is sensed by SLSTR, detects a total of 280,516 km², 23,017 km² more than SYN 865 nm and 18,932 km² more than

	Fire_cci Algorithm Theoretical Basis Document	Ref.:	Fire_cci_D2.1.2_ATBD_S3_v1.1		
		Issue	1.1	Date	22/04/2020
		Page			19

C3SBA10. It is reasonable to think that, while keeping the same accuracy, it is better to select the band that detects more BA. However, the geolocation errors that might be derived from the resampling of the original SLSTR 500 m into the SYN 300 m grid should be analysed since they could be affecting the accuracy of the delimitation of the burned patches.

Finally, the spatial correlations among datasets were found to be very high (0, Table 5 and Table 6) independently of the bands or datasets that were compared. The lowest spatial correlation was found between OLCI iCOR 753.75 nm and SYN 865 nm ($r^2=0.91$, slope=0.94). Conversely, the highest correlations were found, as expected, between OLCI iCOR 753.75 nm and OLCI iCOR 865 nm ($r^2=0.98$, slope=0.99) and SYN 753.75 nm and SYN 865 nm ($r^2=0.98$, slope=0.99). The high correlations of the NIR band centred at 865 nm of both OLCI iCOR ($r^2=0.93$, slope=0.97) and SYN ($r^2=0.95$, slope=1.00) with the C3SBA10 shows the high probability of generating a quite similar global BA product if the FireCCI51 algorithm is applied without changes to any of them.

5 Conclusion

As it was already mentioned in the introduction, the aim of this document was to see if there were enough arguments to believe that SYN data was not a suitable input for a global BA product. Therefore, its performance was compared to other datasets: OLCI iCOR and C3SBA10, SLSTR TOA discarded from the analysis due to problems with the dataset (see Section 4.1). The results presented in the previous section suggested that SYN data is the best alternative to be the input of the FireCCIS310 global BA product. That decision was based on the following conclusions:

1. Although OLCI iCOR has more valid observations per pixel than SYN, this can be overcome using monthly composites as is shown by the higher accuracy metrics of SYN over OLCI iCOR.
2. Since C3SBA10 already uses OLCI as main input, the use of OLCI iCOR may be considered as redundant. This is due to the fact that the differences of the AC did not significantly affect BA detection.
3. Although in this preliminary analysis the FireCCI51 algorithm was applied without changes, which made SWIR channels perform poorly, the idea is to adapt it to vegetation indices of the SWIR region since it is known to be the most sensitive spectral region for BA detection.

In addition to the conclusions that can be extracted from this document, another reason for selecting SYN is the fact that it is an input for the merging reflectance that is being developed by UPM. Therefore, both BA detection and merging reflectance requirements can be fulfilled by a unique dataset.

	Fire_cci Algorithm Theoretical Basis Document	Ref.:	Fire_cci_D2.1.2_ATBD_S3_v1.1		
		Issue	1.1	Date	22/04/2020
					Page

6 References

- Alonso-Canas, I., & Chuvieco, E. (2015). Global Burned Area Mapping from ENVISAT-MERIS data Remote Sensing of Environment, Remote Sensing of Environment, 163, 140-152. <http://dx.doi.org/10.1016/j.rse.2015.03.011>.
- Birks, A., Caroline, C., Smith D., Dawson D. (2011) SLSTR: Algorithm Theoretical Basis Definition Document for Level 1 Observables, version 2.0. Available at: <https://www.earth.esa.int/documents>
- Chuvieco, E., Yue, C., Heil, A., Mouillot, F., Alonso-Canas, I., Padilla, M., Pereira, J.M., Oom, D., Tansey, K. (2016). A new global burned area product for climate assessment of fire impacts. *Global Ecology and Biogeography* 25, 619-629.
- Chuvieco, E., Lizundia-Loiola, J., Pettinari, M.L., Ramo, R., Padilla, M., Tansey, K., Mouillot, F., Laurent, P., Storm, T., Heil, A., Plummer, S. (2018) Generation and analysis of a new global burned area product based on MODIS 250 m reflectance bands and thermal anomalies. *Earth System Science Data* 10, 2015-2031, <https://doi.org/10.5194/essd-10-2015-2018>
- De Keukelaere, L., Sterckx, S., Adriaensen, S., Knaeps, E., Reusen, I., Giardino, C., Bresciani, M., Hunter, P., Neil, C., Van der Zande D., & Vaiciute D. (2018) Atmospheric correction of Landsat-8/OLI and Sentinel-2/MSI data using iCOR algorithm: validation for coastal and inland waters, *European Journal of Remote Sensing*, 51:1, 525-542, DOI: 10.1080/22797254.2018.1457937
- Hantson, S., Padilla, M., Corti, D., & Chuvieco, E. (2013). Strengths and weaknesses of MODIS hotspots to characterize global fire occurrence. *Remote Sensing of Environment*, 131, 152-159.
- Kobayashi, M., Nemilostiv, Y.P., Zyryanova, O.A., Kajimoto, T., Matsuura, Y., Yoshida, T., Satoh, F., Sasa, K., & Koike, T. (2007). Regeneration after forest fires in mixed conifer broad-leaved forests of the Amur region in far eastern Russia: the relationship between species specific traits against fire and recent fire regimes. *Eurasian Journal of Forest Research*, 10, 51-58.
- Lewis, P., Guanter, L., Saldana, G. L., Muller, J., Watson, G., Shane, N., Kennedy, T., Fisher, J., Domenech, C., Preusker, R., North, P., Heckel, A., Danne, O., Krämer, U., Zühlke, M., Fomferra, N., Brockmann, C., Schaaf, C. The ESA globAlbedo project: Algorithm, 2012 IEEE International Geoscience and Remote Sensing Symposium, 22-27 July 2012, pp 5745-5748.
- Lizundia-Loiola, J.; Otón, G.; Ramo, R.; Chuvieco, E. (2020) A spatio-temporal active-fire clustering approach for global burned area mapping at 250 m from MODIS data. *Remote Sens. Environ.* 236, 111493.
- Roteta, E., Bastarrika, A., Padilla, M., Storm, T., & Chuvieco, E. (2019). Development of a Sentinel-2 burned area algorithm: Generation of a small fire database for sub-Saharan Africa. *Remote sensing of environment*, 222, 1-17.
- Stroppiana, D., Grégoire, J.M., & Pereira, J.M.C. (2003). The use of SPOT VEGETATION data in a classification tree approach for burnt area mapping in Australian savanna. *International Journal of Remote Sensing*, 24, 2131-2151.
- Stroppiana D., Boschetti M. (2019) ESA CCI ECV Fire Disturbance: D1.3 Product Validation Plan, version 1.1. Available at: <https://www.esa-fire-cci.org/documents>

Annex 1 Acronyms and abbreviations

AATSR	Advanced Along-Track Scanning Radiometer
AC	Atmospheric Correction
AOD	Aerosol Optical Depth
ATBD	Algorithm Theoretical Basis Document
AVHRR	Advanced Very High Resolution Radiometer
BA	Burned area
BC	Brockmann Consult GmbH
BRDF	Bidirectional reflectance distribution function
C3S	Copernicus Climate Change Service
C3SBA10	C3S Burned area product version 1.0
CCI	Climate Change Initiative
Ce	Commission error
DC	Dice coefficient
DORIS	Doppler Orbitography and Radiopositioning Integrated by Satellite
ECV	Essential Climate Variable
ENVISAT	Environmental Satellite
ERS	European Remote Sensing satellite
ESA	European Space Agency
FireCCI41	Fire_cci MERIS version 4.1
FireCCI50	Fire_cci MODIS version 5.0
FireCCI51	Fire_cci MODIS version 5.1
FireCCIS310	Fire_cci Sentinel-3 version 1.0
FOV	Field-of-View
FR	Full resolution
GCOS	Global Climate Observing System

GNSS	Global Navigation Satellite System
HS	Hotspot
iCOR	Scene generic tool for atmospheric image correction
IPCC	Intergovernmental Panel on Climate Change
LRR	Laser Retro-Reflector
LTDR	AVHRR Long-Term Data Record
MERIS	Medium Resolution Imaging Spectrometer
MODIS	Moderate Resolution Imaging Spectroradiometer
MWR	Microwave Radiometer
NDVI	Normalized Difference Vegetation Index
NIR	Near-InfraRed
Oe	Omission error
OLCI	Ocean and Land Colour Instrument
PRM	Progress Review Meeting
QA	Quality Assessment
relB	Relative Bias
RR	Reduced resolution
S-3	Sentinel-3
SLSTR	Sea and land Surface Temperature Radiometer
SPOT	Satellite Pour l'Observation de la Terre
SRAL	SAR Radar Altimeter
SWIR	Short-Wave InfraRed
SYN	Synergy
TOA	Top of Atmosphere
UPM	Universidad Politécnica de Madrid
VGT	Vegetation
VZA	View Zenith Angle

Annex 2 Accuracy measures for the sample of 2019

Table 4. Estimated accuracy of each dataset and band.

Region	Product	Ce	Oe	DC	relB
California	OLCI iCOR 75.75 nm	41.01%	40.79%	59.10%	0.37%
	OLCI iCOR 865 nm	42.54%	39.06%	59.15%	6.06%
	SYN SDR 753.75 nm	36.00%	42.59%	60.53%	-10.31%
	SYN SDR 865 nm	34.94%	40.72%	62.04%	-8.89%
	SYN SDR 868 nm	42.53%	40.16%	58.63%	4.11%
	SYN SDR 1613.4 nm	56.39%	84.06%	23.34%	-63.46%
	SYN SDR 2255.7 nm	70.20%	92.21%	12.35%	-73.86%
	OLCI C3SBA10 865 nm	35.41%	40.09%	62.16%	-7.25%
Canada	OLCI iCOR 75.75 nm	32.64%	26.83%	70.14%	8.63%
	OLCI iCOR 865 nm	32.62%	27.91%	69.65%	6.98%
	SYN SDR 753.75 nm	34.07%	24.70%	70.30%	14.22%
	SYN SDR 865 nm	34.42%	26.90%	69.13%	11.47%
	SYN SDR 868 nm	36.15%	30.99%	66.33%	8.08%
	SYN SDR 1613.4 nm	31.55%	98.06%	3.78%	-97.16%
	SYN SDR 2255.7 nm	100.00%	100.00%	0.00%	-100.00%
	OLCI C3SBA10 865 nm	34.01%	21.54%	71.69%	18.90%
Australia	OLCI iCOR 75.75 nm	27.54%	42.68%	64.00%	-20.89%
	OLCI iCOR 865 nm	28.81%	41.56%	64.19%	-17.91%
	SYN SDR 753.75 nm	20.59%	37.94%	69.67%	-21.85%
	SYN SDR 865 nm	21.12%	35.93%	70.71%	-18.77%
	SYN SDR 868 nm	24.11%	31.02%	72.27%	-9.11%
	SYN SDR 1613.4 nm	22.53%	57.64%	54.77%	-45.32%
	SYN SDR 2255.7 nm	43.83%	98.24%	3.42%	-96.86%
	OLCI C3SBA10 865 nm	19.96%	35.36%	71.52%	-19.24%
Colombia	OLCI iCOR 75.75 nm	----	----	----	----
	OLCI iCOR 865 nm	----	----	----	----
	SYN SDR 753.75 nm	----	----	----	----
	SYN SDR 865 nm	----	----	----	----
	SYN SDR 868 nm	----	----	----	----
	SYN SDR 1613.4 nm	----	----	----	----
	SYN SDR 2255.7 nm	----	----	----	----
	OLCI C3SBA10 865 nm	----	----	----	----
Central Africa	OLCI iCOR 75.75 nm	5.77%	47.01%	67.84%	-43.77%
	OLCI iCOR 865 nm	6.58%	46.65%	67.92%	-42.89%
	SYN SDR 753.75 nm	4.75%	47.38%	67.79%	-44.76%
	SYN SDR 865 nm	4.82%	47.54%	67.64%	-44.88%
	SYN SDR 868 nm	7.81%	47.72%	66.72%	-43.29%
	SYN SDR 1613.4 nm	4.22%	57.05%	59.31%	-55.15%
	SYN SDR 2255.7 nm	0.94%	84.73%	26.45%	-84.59%
	OLCI C3SBA10 865 nm	7.08%	46.36%	68.02%	-42.28%

Region	Product	Ce	Oe	DC	relB
Angola	OLCI iCOR 75.75 nm	24.10%	33.16%	71.08%	-11.94%
	OLCI iCOR 865 nm	23.36%	33.10%	71.44%	-12.71%
	SYN SDR 753.75 nm	23.51%	29.72%	73.26%	-8.12%
	SYN SDR 865 nm	22.33%	29.73%	73.78%	-9.53%
	SYN SDR 868 nm	28.46%	29.73%	70.90%	-1.78%
	SYN SDR 1613.4 nm	18.98%	72.84%	40.69%	-66.48%
	SYN SDR 2255.7 nm	39.18%	99.86%	0.29%	-99.76%
	OLCI C3SBA10 865 nm	24.02%	28.34%	73.76%	-5.68%
Kazakhstan	OLCI iCOR 75.75 nm	15.46%	38.69%	71.07%	-27.48%
	OLCI iCOR 865 nm	15.28%	41.52%	69.20%	-30.97%
	SYN SDR 753.75 nm	15.58%	51.61%	61.52%	-42.69%
	SYN SDR 865 nm	17.95%	46.63%	64.67%	-34.95%
	SYN SDR 868 nm	19.29%	39.04%	69.46%	-24.47%
	SYN SDR 1613.4 nm	18.16%	73.05%	40.55%	-67.07%
	SYN SDR 2255.7 nm	75.75%	99.76%	0.47%	-99.02%
	OLCI C3SBA10 865 nm	13.89%	43.50%	68.23%	-34.39%
Amur	OLCI iCOR 75.75 nm	13.46%	49.52%	63.76%	-41.67%
	OLCI iCOR 865 nm	14.53%	46.87%	65.53%	-37.84%
	SYN SDR 753.75 nm	20.63%	44.13%	65.58%	-29.61%
	SYN SDR 865 nm	23.58%	41.31%	66.39%	-23.20%
	SYN SDR 868 nm	25.73%	42.78%	64.64%	-22.95%
	SYN SDR 1613.4 nm	39.59%	69.12%	40.87%	-48.88%
	SYN SDR 2255.7 nm	29.75%	86.11%	23.19%	-80.23%
	OLCI C3SBA10 865 nm	14.68%	41.30%	69.55%	-31.20%
Global	OLCI iCOR 75.75 nm	26.06%	37.63%	67.66%	-15.64%
	OLCI iCOR 865 nm	26.49%	37.60%	67.50%	-15.12%
	SYN SDR 753.75 nm	23.70%	36.09%	69.56%	-16.23%
	SYN SDR 865 nm	23.77%	34.84%	70.26%	-14.53%
	SYN SDR 868 nm	26.87%	32.37%	70.27%	-7.52%
	SYN SDR 1613.4 nm	21.62%	69.95%	43.45%	-61.66%
	SYN SDR 2255.7 nm	40.69%	98.59%	2.76%	-97.62%
	OLCI C3SBA10 865 nm	23.28%	32.99%	71.54%	-12.65%

Annex 3 Intercomparison

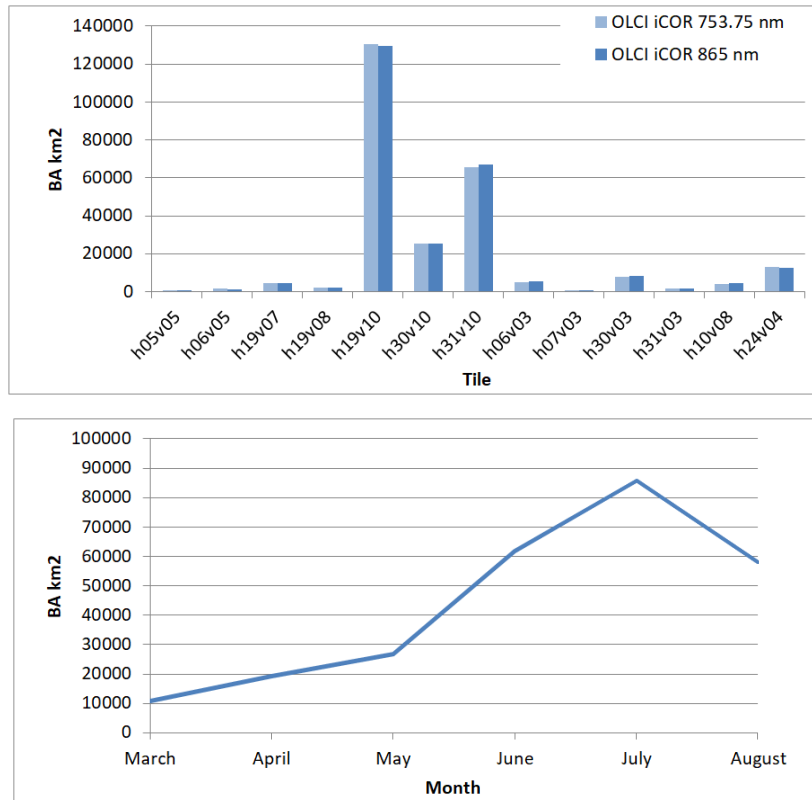


Figure 8. BA in km² per tile (top) and month (down) detected by each band of the OLCI iCOR product.

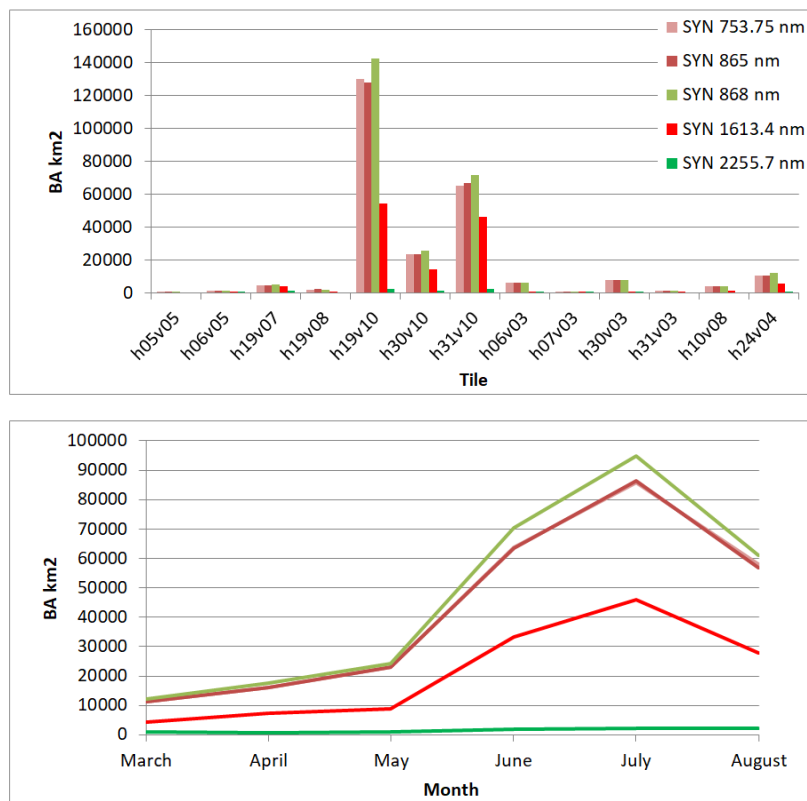


Figure 9. BA in km² per tile (top) and month (down) detected by each band of the SYN product.

Table 5. R2 of the spatial correlation between datasets.

R2	OLCI iCOR 753.75nm	OLCI iCOR 865 nm	SYN 753.75 nm	SYN 865 nm	SYN 868 nm	OLCI C3SBA10 865 nm
OLCI iCOR 753.75nm		0.98	0.92	0.91	0.92	0.92
OLCI iCOR 865 nm			0.93	0.92	0.92	0.93
SYN 753.75 nm				0.98	0.97	0.95
SYN 865 nm					0.97	0.95
SYN 868 nm						0.95
OLCI C3SBA10 865 nm						

Table 6. Slope of the spatial correlation between datasets.

Slope	OLCI iCOR 753.75nm	OLCI iCOR 865 nm	SYN 753.75 nm	SYN 865 nm	SYN 868 nm	OLCI C3SBA10 865 nm
OLCI iCOR 753.75nm		0.99	0.95	0.94	1.01	0.97
OLCI iCOR 865 nm			0.95	0.94	1.01	0.97
SYN 753.75 nm				0.99	1.05	0.99
SYN 865 nm					1.06	1.00
SYN 868 nm						0.93
OLCI C3SBA10 865 nm						